Strong-Field Ionization of Lithium

Michael Schuricke,[1] Ganjun Zhu,[1] Jochen Steinmann,[1] Konstantinos Simeonidis,[1] Igor Ivanov,[2] Anatoli Kheifets,[2] Alexei N. Grum-Grzhimailo,[3] Klaus Bartschat,[4] Alexander Dorn,[1] and Joachim Ullrich[1]

[1]*Max-Planck-Institut für Kernphysik, Saupfercheckweg 1, 69117 Heidelberg, Germany*
[2]*Research School of Physical Sciences and Engineering,*
Australian National University, Canberra, ACT 0200, Australia
[3]*Institute of Nuclear Physics, Moscow State University, Moscow 119991, Russia*
[4]*Department of Physics and Astronomy, Drake University, Des Moines, Iowa 50311, USA*
(Dated: September 3, 2010)

We report photoelectron energy spectra, momentum, and angular distributions for the strong-field single ionization of lithium by 30 femtosecond laser pulses. For peak intensities between 10^{11} and 10^{14} W/cm^2 at a central wavelength of 785 nm, the classical over-the-barrier intensity was reached well inside the multiphoton regime. The complete vector momenta of the ionization fragments were recorded by a reaction microscope with a magneto-optically trapped target (MOTREMI). On the theoretical side, the time-dependent Schrödinger equation was solved by two independent methods seeking the solution directly on a radial grid. Distinct differences between the results of both calculations and also in comparison with experiment point to a high sensitivity of this reaction with respect to small details, particularly in the description of the Li+ core.

I. INTRODUCTION

Atomic ionization in a strong electromagnetic field is a highly non-linear process, which manifests itself in such phenomena as multiphoton ionization (MPI), above threshold ionization (ATI), and high harmonic generation (HHG). Over the past three decades, since sufficiently intense laser sources became available, the interest in these phenomena has grown considerably. The available literature on this topic is enormous. This makes it difficult to direct the reader to any single comprehensive review. Some insight into the problem can be gained from a number of review papers [1–4].

Various regimes of strong-field atomic ionization can be conveniently categorized by the adiabaticity Keldysh parameter, which relates the time-scales or frequencies of atomic motion and the laser field $\gamma = \omega/\omega_{\text{tunnel}}$ [5]. Alternatively, the Keldysh parameter can be expressed in terms of the atomic ionization potential IP and the ponderomotive potential U_p, $\gamma = \sqrt{\text{IP}/2U_p}$. The MPI regime is characterized by $\gamma \gg 1$. Here, the characteristic tunneling time of the atomic electron over the Coulomb barrier $\omega_{\text{tunnel}}^{-1}$ is much larger than the oscillation period of the electromagnetic field ω^{-1}. Such a fast ionization process should be considered using the quantum-mechanical language of simultaneous absorption of several laser photons. The opposite limit of $\gamma \ll 1$ is reached when the laser field is changing slowly as compared to the characteristic tunneling time. Such a slow, adiabatic process can be described quasi-classically using the language of field strength and electron trajectories driven by this field [6].

The transition between the MPI and tunneling regimes is characterized by radical changes in the photoelectron energy spectra [7]. The periodical structure of narrow Stark-induced resonances [8] and above-threshold ionization disappears gradually, thus transforming itself into a structureless continuum.

This simple picture can be complicated by another strong-field ionization phenomenon known as over-the-barrier ionization (OBI). With increasing field strength and intensity, the width and height of the atomic Coulomb barrier is reduced until it is completely suppressed by the external field. The corresponding field intensity can be estimated as $I_{\text{OBI}} = \text{IP}^4/16Z^2$ [9]. Such a barrier suppression takes place independently of the value of the Keldysh parameter. In the sequence of noble gas atoms at the laser field parameters considered by Mevel et al. [7], OBI was occurring well into the tunneling regime.

This, however, is not a universal rule. The lithium atom driven by a femtosecond laser in the visible light spectral range exhibits an unusual example of OBI in the entirely quantum MPI regime [10]. Such an OBI process cannot be treated quasi-classically and analyzed in convenient terms of competing electron trajectories. Instead, a full quantum-mechanical treatment should be given. Because of the large field intensity, such a treatment should be non-perturbative and explicitly time-dependent. Given a large number of field oscillations in the laser pulse and the complexity of the target, an accurate theoretical description of the MPI of Li becomes a challenging task.

The photoelectron energy distribution is not the only sensitive probe of strong-field atomic ionization. More detailed information on electron dynamics and ionization mechanisms can be gained by studying the corresponding photoelectron angular distribution (PAD). First investigations of multiphoton PADs revealed intensity-dependent structures [11]. Since the PADs were more and more elongated towards the polarization axis of the laser field with increasing photon order of the process, this was interpreted as occupation of final states with higher angular momentum. A more complicated experimental situation was soon encountered with the appearance of additional structures referred to as side lobes [12] and jets [13]. These structures appeared at characteristic regions in the ATI photoelectron spectra, depending on the ponderomotive energy. In addition, PADs were used to identify the resonant ionization processes involving high-lying Rydberg states ("channel switching") [14].

In the early experiments [11–13], PADs were detected by varying the angle between the polarization axis of the laser

light and the detection axis of the time-of-flight spectrometer. Recently, more sophisticated measurements became possible using the Reaction Microscope (REMI) technique [15, 16]. In REMI experiments, two components of the photoelectron momentum, parallel and perpendicular to the polarization axis of laser, are detected simultaneously. This provides ample information on both, the energy and angular distributions of photoelectrons. Analogous information is detected in the ion channel as well. In a single ionization process, because of momentum conservation, the ion channel should mirror the electron channel. This can be used to check the consistency of the measurement and to reduce background.

The advantages of the REMI technique became obvious when rich momentum-space structures were revealed in the strong-field ionization of noble-gas atoms studied in the transitional $\gamma \sim 1$ regime [15, 16]. Surprisingly, the remnants of the MPI rings and ubiquitous fan-like structures were seen well outside of the MPI domain. Now this effect is well understood and attributed to the long-range Coulomb interaction between the tunnel-ionized electron and the target ion it has left behind [17, 18]. The fan-like structures survive the integration over the laser focus volume, as shown in recent comparison between theoretical predictions with experimental data [19]. This is explained by the dominant contributions of a few characteristic angular momenta, which vary insignificantly with the laser field intensity [20].

In the present work, we apply the REMI technique to study strong-field ionization of the lithium atom deep inside the MPI regime. This is the first experimental investigation of this kind as it combines the sophisticated detection and target preparation techniques with the unique strong-field ionization regime. We reach the over-the-barrier laser intensity I_{OBI} well and truly inside the MPI regime.

These experimental efforts are matched by adequate theoretical tools involving the solution of the time-dependent Schrödinger equation (TDSE). In the present paper, two independent approaches are employed. The first one uses a direct grid-based approach in connection with the matrix iteration method (MIM) of Nurhuda and Faisal [21]. In a recent publication [22], the applicability of this method was demonstrated for a numerically challenging problem of the atomic hydrogen driven by a strong laser pulse with peak intensities reaching up to 10^{15}W/cm^2. For the present work, this approach was modified to account for the more complex Li structure. Finally, we applied a similar model employing a different target potential and the Arnoldi-Lanczos method (ALM) [23] for time propagation of the TDSE in order to elucidate the sensitivity of the results to these details.

II. EXPERIMENTAL SETUP

The presented results were obtained by applying a novel apparatus, combining for the first time a full Reaction Microscope (REMI) [37] for momentum resolved ion and electron detection with a magneto optical trap (MOT) target dubbed MOTREMI.

Since only a brief review of the apparatus was given previously [24],we provide a more detailed description here. On the one hand, the individual systems, the REMI and the MOT, are standard techniques nowadays and hence a fair amount of literature is available. The reader is referred to [25, 26] for a review on REMIs and MOTs, respectively. On the other hand, the merging of these two state-of-the-art technologies holds great technical challenges, as the requirement for precisely known homogeneous electric and magnetic fields for guiding and imaging of the charged particles in a REMI is inherently incompatible with the magnetic gradient field and a local field minimum required for the MOT operation. Thus, we apply a measurement cycle during which the MOT is switched off, thus releasing the atoms for a few milliseconds to allow for the REMI operation. Subsequently the atoms are recaptured. While this makes it possible to obtain well-resolved ion-momentum data, the more critical electron-momentum measurement requires MOT off-times beyond 4 ms, thereby making recapturing inefficient. Hence, the electron spectra presented below were obtained using the hot Li beam from the oven as a target, which is normally used for MOT loading. Due to its low beam density of about 10^7cm^{-3} this is only feasible for high intensities of the ionizing laser pulse above $I_p = 4 \times 10^{12}$ W/cm^2 where the ionization rate is large. In the future we plan to overcome this problem by transferring the atoms from the MOT into an intense, far red-detuned laser beam waist, where they are trapped by means of dipole forces. Thus, magnetic field-free trapping will allow for high resolution electron momentum detection as well as higher experimental duty cycles.

In the following sections the REMI and the MOT including the applied switching sequence are described. Finally the ionizing laser parameters and the intensity calibration will be elucidated.

A. Reaction Microscope

A schematic view of the experimental setup is shown in Fig. 1. The target region is immersed in a homogeneous electric field between 0.4 V/cm and 0.6 V/cm, which accelerates ions and electrons into opposite directions along the spectrometer axis toward two detectors.

The spectrometer has an inner free diameter of 83 mm and a total length of 107 cm divided into acceleration and drift regions for ions and electrons. The electron side is set up in the Wiley-Mclaren or time focusing configuration. On the ion side a 3D focusing geometry is applied, i.e., time and position focusing of ions with identical momentum but originating from an extended source volume. The ion spectrometer is 77 cm long instead of 30 cm on the electron side, resulting in a longer time-of-flight and, therefore, in a better ion momentum resolution. The gold plated $\mathrm{AlMg_3}$ electrodes leave rectangular openings of 30x200 mm at the sides of the spectrometer and a round opening at the top and bottom of it, thus providing easy access for the MOT lasers and also for projectiles of any kind. Time and position sensitive detectors are realized via a stack of multichannel plates (MCP) in chevron configuration and delay line anodes.
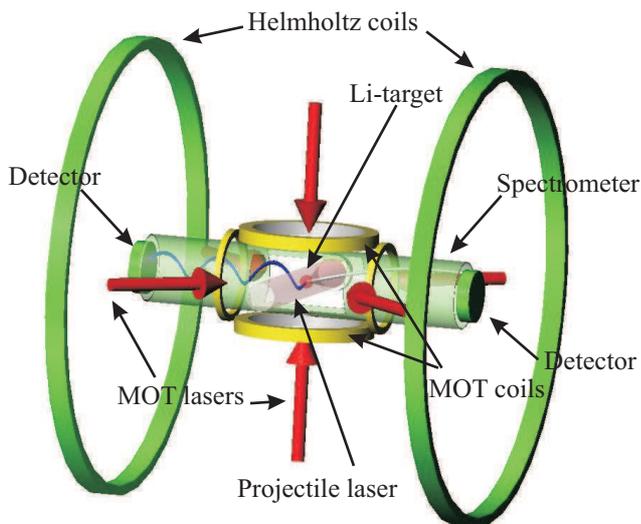
FIG. 1: Schematic view of the experimental setup. The lithium atoms are trapped in the center of the spectrometer and subsequently ionized by the back-reflected fs-laser pulses. Weak electric and magnetic fields, produced by the spectrometer electrodes and the Helmhotlz coils, respectively, guide the ionization fragments to time and position sensitive detectors.

In addition to the electric extraction field a magnetic field of approximately 3 G is applied along the spectrometer axis. It confines the electron trajectories transversally as indicated by the helix trajectory in Fig. 1 and is generated by a pair of large Helmholtz coils ensuring its homogeneity over the entire volume of the electron spectrometer. To compensate for the components of the Earth's magnetic field perpendicular to the spectrometer axis two additional coil pairs in Helmholtz configuration are used (not shown in the figure). The complete setup, except for the Helmholtz coils, is settled inside a UHV-chamber, where pressures around 1×10^{-10} mbar are routinely achieved. From their times-of-flight and positions the 3D-vector momenta of ions or electrons were determined over the whole solid angle with a resolution of $\Delta p_{\mathrm{R,longitudinal}} = 0.04$ a.u. ($\Delta p_{\mathrm{R,transversal}} = 0.08$ a.u.) for the recoil ions and $\Delta p_{\mathrm{e,longitudinal}} = 0.015$ a.u. ($\Delta p_{\mathrm{e,transversal}} = 0.03$ a.u.) for the photoelectrons, respectively. Regarding single ionization, the recoil ions and the photoelectrons are imprinted with the same momentum but opposite signs. Hence, the gathered information is complementary and the detection of either corresponds to a kinematically complete experiment. In case of the electron spectra presented here the lithium atoms were ionized from the thermal beam emerging from the Zeeman slower. Although the high temperature of the atoms degraded the momentum resolution of the ions, they were still used as coincident trigger for the electron detection.

B. Magneto-optical trap

For target provision a three-beam magneto optical trap is used consisting of an atomic beam for loading, a pair of mag-

netic field coils in anti-Helmholtz configuration, and counter-propagating laser beams along three spatial axes perpendicular to each other. Up to 6×10^7 atoms could be trapped with temperatures below 1 mK corresponding to a thermal momentum spread below 0.01 a.u.

The MOT is loaded with ^{7}Li atoms emerging from an oven with a temperature of approximately 700 K. The atoms are decelerated in a Zeeman slower (both not shown in Fig. 1) before entering the main chamber, where those traversing the MOT capture radius are trapped.

The anti-Helmholtz coils are mounted intra vacuum and are built using an insulated hollow copper tube of 5 mm diameter and 1 mm wall thickness allowing for external water cooling. Each coil has 24 windings with an inductance of 75 μH per coil. They are placed 10 cm apart of each other and produce a magnetic gradient field of 0.282 G/(cm $\times$ A) in the axial direction. For the data presented here the coils were usually operated at a coil current of 35 A, corresponding to a gradient field of approximately 10 G/cm in axial direction.

The MOT laser beams are realized using a diode laser (Toptica DL100) in conjunction with a tapered amplifier (Toptica TA100). Thereby, the DL100 serves as master laser and is locked to the crossover frequency of the $F = 2 \rightarrow F = 3$ and the $F = 1 \rightarrow F = 2$ hyperfine transitions within the D2 line of ^{7}Li through absorption spectroscopy in a vapor cell. The beam is then amplified in the TA100 providing a laser power of 400 mW. Subsequently, the beam is split into two parts and frequency shifted by means of two computer controlled 200 MHz acousto-optic modulators (AOMs) in double pass configuration. These shift the frequencies to the $^2 S_{1/2}(F = 2) \rightarrow ^2 P_{3/2}(F = 3)$ cooling and the $^2 S_{1/2}(F = 1) \rightarrow ^2 P_{3/2}(F = 2)$ repumping transitions, respectively. They also introduce a small red detuning of $\delta \approx 3 \times \Gamma$, with Γ being the natural line width. Thereafter the two beams are overlapped again and the largest fraction, approximately 170 mW, is used for the MOT beams. The remaining beam with 30 mW power is frequency shifted by another AOM and used for the Zeeman slowing of the atoms.
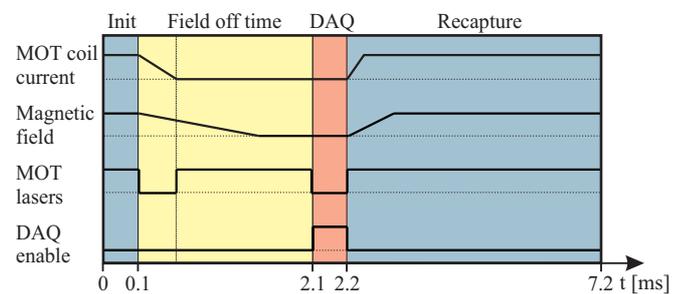
FIG. 2: Timing scheme of the measurement cycle.

As indicated above, for the recoil-ion momentum measurements the MOT is operated in a switched cycling mode employing synchronized switching of the trapping lasers, the MOT coils as well as triggering and gating of the data acquisition. Therefore, the setup is controlled by a real-time system of type ADwin Gold (Jäger GmbH) with a time resolution of 10 μs. After 5-10 s loading of the MOT the oven

beam is blocked by a mechanical shutter, the magnetic field and the laser of the Zeeman slower are switched off, and the experiment-control enters the measurement cycle, for which the most important parameters are shown in Fig. 2. The MOT magnetic field and the MOT lasers are switched off simultaneously. Two hundred microseconds later the lasers are turned on again to form an optical molasses, which slows down the expansion of the atomic cloud. Keeping the lasers on while switching the coils would result in the destruction of the thermal cloud due to the changes in the Zeeman splitting of the atoms, resulting in a strong absorption of the trapping laser light due to the local magnetic field. At $\tau = 2$ ms, i.e., the time of arrival of the projectile pulse, the MOT lasers are switched off and data acquisition is enabled for a time period slightly longer than the flight times of the ions. Finally, essentially all atoms are recaptured and recompressed in the MOT for approximately 5 ms. This procedure allows for up to 1500 release-recapture cycles before reloading from the oven beam is required.

The rather long delay between switching off the MOT and data taking is required to allow for the decay of magnetic fields. The switching of the coil current itself can be achieved on a time scale of several hundred microseconds or below (depending on the inductivity of the coils and the switch). In our case the MOT coil current is controlled via an Insulated Gate Bipolar Transistor (IGBT) of type EUPEC FZ 800 R16 KF4, achieving a switch-off time of 400 μs. Great care has been taken to minimize eddy current induction in our setup. As already mentioned previously, the anti-Helmholtz coils are built intra-vacuum to keep them small and their inductivity low. Moreover, all parts mounted in the vacuum chamber, e.g., the electrodes of the spectrometer, the drift tubes and the rims for the coils, are cut at least once, to prevent closed conducting loops. However, it appeared that despite the careful design eddy currents emerged in the chamber walls. Test experiments with a variable delay τ between switching off the coil current and the ionizing laser pulse revealed that only for $\tau \geq 4$ ms the eddy current induced B-fields do not deteriorate the electron momentum spectra. However, for such long off-times the atomic cloud has expanded significantly, thus resulting in low target density and low recapture efficiency even if optical molasses cooling is applied. Thus, so far the measurement of high-resolution coincident ion- and electron spectra could not be achieved.

C. The Femtosecond Laser Pulses

The ionizing femtosecond laser pulses were supplied by a laser system from KM labs consisting of a type MTS-1 laser oscillator amplified by a KML Dragon system by means of chirped pulse amplification. This setup produced linearly polarized laser pulses of 30 fs duration, at a central wavelength of 785 nm (photon energy $E_{\mathrm{ph}} = 1.58$ eV) with a repetition rate of 8 kHz. The laser polarization was cleaned using four thin beam splitters (pellicles) under the Brewster angle, and the laser intensity was reduced by another four coated pellicles, each reflecting up to 45% of the incoming beam,

and a reflective filter. All elements were pre-compensated in the grating compressor following the laser amplifier for their second-order dispersion. Inside the vacuum chamber the beam was focused by a silver plated retro-reflecting mirror, mounted on a linear manipulator, with a focal distance of $f = 75.0$ mm, resulting in a focus of 20 μm waist radius. Thereby peak intensities between $I_p = 4 \times 10^{11}$ W/cm^2 and $I_p = 10^{14}$ W/cm^2 were reached.

The laser peak intensity was calibrated, according to Alnaser *et al.* [27], by monitoring the branching ratios of the various dissociation channels of H_2 in the residual gas. These branching ratios change characteristically between a peak intensity of $I_p = 1 \times 10^{14}$ W^2 and $I_p = 6 \times 10^{14}$ W/cm^2. Therefore, the linearly polarized projectile laser was focused in the chamber for various intensities in this regime, and time-of-flight spectra were recorded. By comparison of the obtained spectra with those published in [27] a proportionality factor between the time-averaged power of the laser and the absolute peak intensity was obtained, which should be accurate to at least 50%. During the experiment the laser power was monitored via a photodiode, whose signal was read into an ADC and recorded for every single event. Thus, we assume that the data presented below have an absolute error in intensity of no more than 50% and that the relative intensities did not vary by more than $\pm 10\%$.

III. THEORY

As mentioned in the Introduction, we employed two independent methods for the numerical solution of the TDSE describing the response of the Li atom to a strong laser field. The key elements of these methods are summarized below.

A. The matrix iteration method (MIM)

The MIM approach was described in detail in a recent paper for ionization of atomic hydrogen in a strong laser field [22]. Briefly, the Crank-Nicholson approximation

$$\boldsymbol{a}(t + \Delta) = \frac{1 - i\boldsymbol{H}(t + \Delta/2)\Delta/2}{1 + i\boldsymbol{H}(t + \Delta/2)\Delta/2}\boldsymbol{a}(t) + O(\Delta^3). \quad (1)$$

to the time evolution operator is made [28]. Here $\boldsymbol{H}(t)$ consists of the time-independent field-free Hamiltonian plus the interaction with the time-dependent electric field treated in the dipole approximation.

The inverse of the operator $1 + i\boldsymbol{H}(t + \Delta/2)\Delta/2$ is evaluated by the matrix iteration algorithm of Nurhuda and Faisal [21]. The key point is to split the entire operator into diagonal (O_D) and off-diagonal ($\boldsymbol{O}_{ND}$) parts and then to use a rapidly converging series expansion in terms of $\boldsymbol{O}_{ND}\boldsymbol{O}_D^{-1}$. Note that the inverse of $\boldsymbol{O}_D$ is trivial, and the convergence can be guaranteed (and monitored) due to the appearance of the time step Δ in the off-diagonal matrix $\boldsymbol{O}_{ND}$. While the finite-difference evaluations of the derivative operators require a smaller radial step size (we used 0.02 a.u.) than in basis-set

methods, the advantages of the approach lie in the fact that it can be applied without change and serious loss of accuracy over a large range of energies and a wide radial grid (we used $R_{\max} = 3000$ a.u. for the highest intensities), thereby ensuring that edge effects such as reflection either do not appear at all or can easily be controlled by an absorbing potential.

As mentioned earlier, for high laser intensities such as those achieved in the present experiment, it is very difficult to obtain partial-wave converged results if the length-form of the electric dipole operator is employed. Since the length form gives accurate results for low peak intensities, we decided to perform calculations for peak field strengths from $0.001 - 0.010$ a.u. (corresponding to peak intensities between $3.5 \times 10^{10} - 3.5 \times 10^{12}$ W/cm^2) with the length form using the method described by Grum-Grzhimailo *et al.* [29] and from $0.010 - 0.070$ a.u. (the latter corresponding to 2.5×10^{14} W/cm^2) with the velocity form of the dipole operator. The results at the switching point of 0.010 a.u. agreed very well with each other, thus giving us confidence in the numerical accuracy of our approach. We used partial waves up to $L_{\max} = 30$ for the calculations in the length form and up to $L_{\max} = 20$ in the velocity form. The convergence of the results was checked carefully and found to be excellent.

Finally, the Li target was treated as a quasi-one electron atom, with the $1s^2$ core described by a local potential that included the static potential as well as polarization and exchange terms. While only an approximation to the true non-local potentials obtained in an all-electron treatment with open core, such local potentials often provide a very convenient and sufficiently accurate representation of the basic physics (exchange and polarization) associated with the core. We used the program published by Bartschat [30] to obtain this potential, which reproduced the binding energies in the Rydberg series of the Li atom to an accuracy of better than one percent for principal quantum numbers up to $n = 12$. This could be further improved by using ℓ-dependent potentials [31], which was not done in the present work. The distorted waves for projecting the final wave function were also calculated in this potential.

B. Arnoldi-Lanczos method (ALM)

The MIM method used a model local Hamiltonian that included the static, polarization and exchange potentials. In order to elucidate to which extend the calculated spectra depend on these details we have performed a second calculation, referred to as ALM below. This calculation employs a finite-difference technique to solve the TDSE, closely resembling the MIM calculation described above. The differences in the choice of the model target potential were as follows. In the ALM calculation, we used the so-called parametrized optimized effective potential [32] given by the effective potential method [33]. This method provides a variational approximation to the many-electron problem using single-particle wave functions as a variational ansatz. The single-particle orbitals satisfy a single-particle Schrödinger equation with a local potential. The precise form of this potential is determined varia-

tionally. For the potential thus obtained, the ground-state energy is an upper bound to the exact energy and is above the Hartree-Fock value [32].

We used the Arnoldi-Lanczos method (hence the acronym ALM) [23] for time-propagating the solution of the TDSE with the local Hamiltonian supplied by the effective potential method. The ALM method represents the wave function at a time $t + \Delta t$ as a vector from the Krylov subspace, formed by the vectors $\Psi(t), \hat{H}\Psi(t), \ldots \hat{H}^m \Psi(t)$. The procedure is unconditionally stable and explicit, which is a convenient feature allowing to treat efficiently large scale problems. Convergence of the calculation with respect to the dimension of the Krylov subspace was checked. It was found that the choice of $m = 5$ and the time-step $\Delta = 5 \times 10^{-3}$ a.u. gave an accurate solution of the TDSE.

We used the velocity gauge to describe the atom-field interaction. The system was enclosed in a box of size of 2000 a.u. On the outer boundary of the box the so-called transparent boundary condition [34] was imposed. As in the MIM calculation, we included terms with angular momenta up to 20 in the partial-wave expansion for the wave function. The electron distribution functions were computed by projecting the solution of the TDSE after the end of the pulse on the ingoing distorted waves calculated in the same effective potential.

C. Focal Volume Averaging

The theoretical methods described above provide information on the ionization rate, the energy E_e, and the emission angle θ_e of electrons ionized during the laser pulse, for a single atom and a given peak intensity I_p. The temporal profile of the real laser pulse is accounted for by a (co)sine-squared envelope of the electric field. For comparison with experiment, however, one has to also consider the spatial distribution of the laser peak intensities. As the target is far more extended than the laser focus, ions and electrons will emerge from different origins inside the interaction volume, experiencing different laser peak intensities. Thus, the theoretical results cannot be compared directly with the experimental data, but instead have to be averaged over the laser intensities present in the target region. We therefore weighted the ionization rates calculated for a number of peak intensities according to the volumes of the respective iso-intensity shells in the laser focus and added all contributions. The probability $P^{\text{av.}}(I, E_e, \theta_e)$ to detect an electron with a certain energy and angle is then given by

$$P^{\text{av.}}(I, E_e, \theta_e) = \rho \sum_k P_k^{\text{theo}}(I_p, E_e, \theta_e) V_k. \quad (2)$$

Here ρ denotes the target density and V_k the volume of an iso-intensity shell, which is given by [35]

$$V_k = \pi \omega_0 z_r \left\{ \frac{4(c_1 - c_2)}{3} + \frac{2(c_1^3 - c_2^3)}{9} \right.$$
$$\left. - \frac{4}{3} \tan^{-1}(c_1) - \tan^{-1}(c_2) \right\}, \quad (3)$$

(a)

$I_p = 4 \cdot 10^{11}\,\mathrm{W/cm^2}$ $U_p = 0.02$ eV
$= 0.06 \cdot I_{OBI}$ $\gamma = 11.6$

(b)

$I_p = 8 \cdot 10^{11}\,\mathrm{W/cm^2}$ $U_p = 0.04$ eV
$= 0.24 \cdot I_{OBI}$ $\gamma = 8.2$

(c)

$I_p = 2 \cdot 10^{12}\,\mathrm{W/cm^2}$ $U_p = 0.12$ eV
$= 0.59 \cdot I_{OBI}$ $\gamma = 4.7$
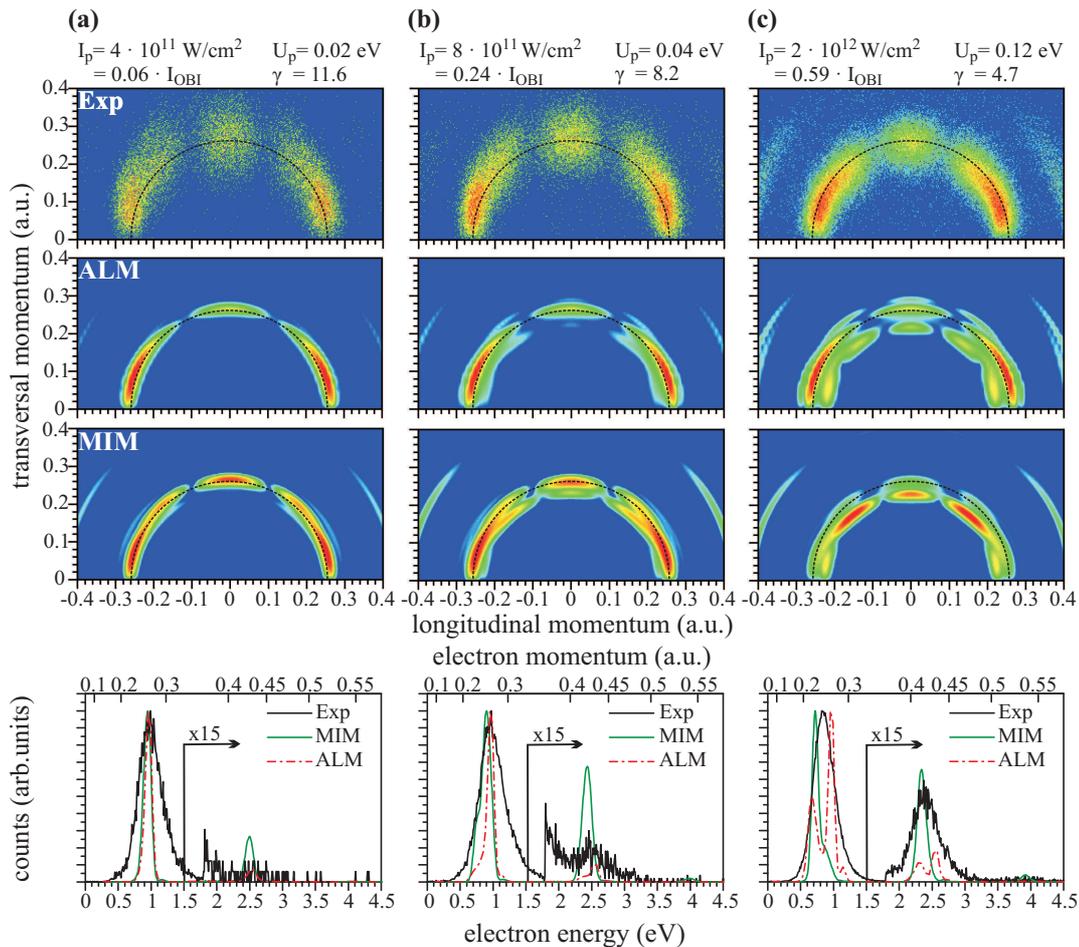
FIG. 3: Top three rows: Electron momentum distribution parallel (longitudinal) and transversal (perpendicular) to the laser polarization direction. First row: experimental data obtained by recoil-ion momentum detection. Second and third rows: calculated spectra using the ALM (second row) and MIM (third row) models, respectively. The laser pulse peak intensity I_p, the ponderomotive potential U_p, and the Keldysh parameter γ are given above each column. The colour scale of the momentum spectra is logarithmic. Dashed semi circle: Nominal position of the four-photon line. Bottom row: Energy spectra extracted from the experimental and theoretical ALM and MIM momentum data. All data are internormalized at the peak of the main MPI line. In these diagrams, the count rates within the marked energy intervals are multiplied by 15.

where $c_j = [(I_p - I_j)/I_j]^{-1/2}$ with the peak intensity I_p, w_0 is the waist radius, and z_r is the Rayleigh range of the laser focus. In order to weight the theoretical spectra the target density ρ was assumed to be constant over the laser focus, which is a good approximation for both targets.

Finally, the numerical calculations are performed with a fixed value of the carrier envelope phase. Since this phase is not resolved experimentally, it has to be averaged over as well. Since the laser pulse is relatively long, we performed this averaging by symmetrizing the results obtained for 0° and 180°. This approximation will breakdown at high intensities and very short pulse lengths. Spot checks performed for a few cases, however, confirmed that the procedure is appropriate for all cases presented here.

IV. RESULTS AND DISCUSSION

Figures 3 – 5 display the momentum and extracted energy spectra that were recorded for peak intensities between $I_p = 4 \times 10^{11}$ W/cm² up to $I_p = 7 \times 10^{13}$ W/cm². This range covers the transition from multiphoton to over-the-barrier ionization, which is nominally setting in at $I_p = 3.4 \times 10^{12}$ W/cm² and a Keldysh parameter of $\gamma = 3.7$. The momentum spectra are plotted as function of the longitudinal and transversal momentum with respect to the laser polarization. They are integrated over the azimuthal angle, since the cross section is axially symmetric with respect to the laser polarization. As explained above, the data at lower intensities (Fig. 3) are obtained from recoil-ion momentum measurements using the MOT-target, whereas the high intensity results (Fig. 5) are direct electron momentum measurements with improved resolution. To illustrate this change in resolution, Fig. 4 depicts experimental spectra for both detection
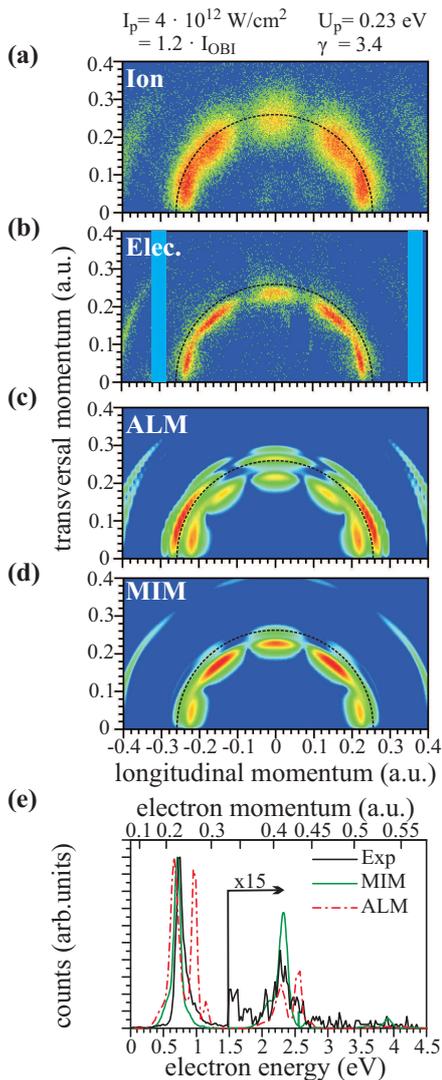
FIG. 4: Continuation of Fig. 3. In addition to the experimental ion momentum spectrum (top panel), we also show the electron momentum spectrum with improved resolution (second panel). Vertical cuts in this diagram mark regions where the electron spectrometer has no resolution in the transverse direction.

methods at $I_p = 4 \times 10^{12}$ W/cm^2.

In addition to the experimental data, the figures contain momentum spectra obtained by the MIM and ALM models as well as the energy spectra (bottom row). Both were averaged over the focal volume of the interaction region. The momentum distributions show ring-like structures corresponding to particular photoelectron excess energies. The energy level diagram (Fig. 6) illustrates that starting from the initial ground state with $E_{ph} = 1.58$ eV at least four photons are required to reach the continuum. In the low-intensity regime, this non-resonant multiphoton ionization (NRMPI) is the dominating process. Emanating from the $2s$ ground state, the excess energy of the photoelectrons is expected to be $E_e = 0.92$ eV, in perfect agreement with the observed most likely photoelectron energy and momentum of 0.26 a.u. at low intensity (Fig. 3(a),

top and bottom diagrams).

In the momentum distributions shown in this figure and all figures discussed below, the nominal position of the four-photon line is marked by a dashed semicircle. The observed angular intensity distribution relates to a superposition of the accessible emitted partial waves. In the case of four-photon absorption, s-, d- and g- partial waves can be emitted. Besides NRMPI, already for the lowest intensity considered here, above threshold ionization (ATI), i.e. five-photon absorption, can be identified in the energy spectrum for $E_e = 2.5$ eV. As expected, the relative strength of this line and higher-order ATI-lines increases for rising intensity. In addition, up to $I_p = 4 \times 10^{12}$ W/cm^2 a downward shift of both lines is observed. This can be attributed to the increase of the ponderomotive energy U_p.

Above $I_p = 4 \times 10^{12}$ W/cm^2, the MPI and ATI line energies stay constant. This can be understood in terms of resonance enhanced multi-photon ionization (REMPI). Due to the AC Stark-shift of the atomic state energies, which for the higher levels is close to the ponderomotive upward shift of the ionization potential, the $4p$ and $4f$ states can be resonantly populated by three-photon absorption for $U_p = 0.2$ eV (see Fig. 6). The subsequent one- or multi-photon absorption then leads to ionization. Due to the spatio-temporal intensity distribution of the laser pulses, this process also dominates the spectra for higher intensities. As already mentioned in Sec. III C, all intensities up to the peak intensity are present in the vicinity of the laser focus and in the temporal intensity course. Hence, contributions from an intermediate resonance can also contribute at far higher intensities if the associated resonance intensity is reached in the outer part or in the rising slope of the laser pulse. The excess energy observed, $E_e = 0.73$ eV, is in excellent agreement with ionization through $4l$-intermediate states, as the expected photoelectron energy is in the range of $E_{e,4p-f} = 0.70 - 0.73$ eV.

The spectra with improved experimental resolution, which are available beginning from $I_p = 4 \times 10^{12}$ W/cm^2, confirm the dominance of a single REMPI line. In addition, Fig. 4(b) reveals a faint line on the high momentum side of the main line. Beginning from $I_p = 2 \times 10^{13}$ W/cm^2, a significantly radially broader line is visible on the low momentum side. Both contributions become more pronounced for increasing laser intensity. The energy positions of these side lines were determined by a fitting procedure to be $E_e = 0.41$ eV and $E_e = 1.05$ eV, respectively. A similar three-fold line splitting is observed for the first-order ATI line at high intensity as visible in Fig. 5(c) (top diagram). The fact that the side lines show the same number of angular maxima as the main REMPI line indicates that they are dominated by the same angular momentum of the photoelectron. For the line at 1.05 eV, its position 0.3 eV above the main line, its narrow momentum width, and the stable position in all spectra Fig. 5(a) to (c) suggest that it is associated with the atomic $5f$ state. As the $5f$ state is not accessible via direct MPI from the ground state, particularly when a ponderomotive upward shift is considered, another process must be responsible for its population. In the photon picture this might be explained by a Raman-like process coupling population from the $4p$ and $4f$ levels via a two-
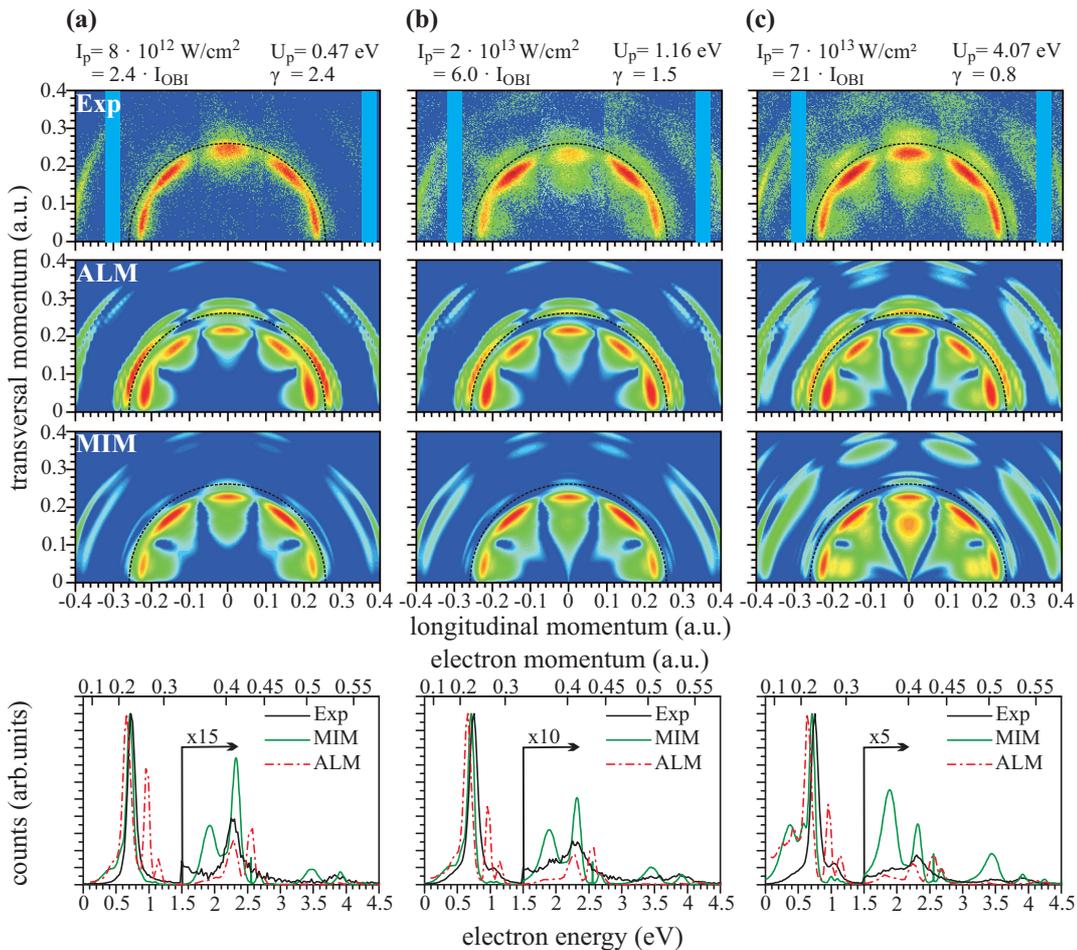
FIG. 5: Continuation of Fig. 4 for higher intensities showing only experimental electron momentum spectra. Vertical cuts in these diagrams mark regions where the electron spectrometer has no resolution in the transverse direction.

photon process through the continuum to the $5f$ state. In the field picture a process similar to frustrated tunneling ionization (FTI) [36] could be considered responsible. As it is the case there the electron starting to propagate over the barrier is recaptured in an excited state due to the combined, dynamic forces of the Coulomb and laser fields.

The low-energy part centered at 0.41 eV cannot be assigned easily to a bound state. For the interpretation of this structure it has to be taken into account that the laser intensities considered here are well beyond the over-the-barrier intensity and the Keldysh parameter is close to or below unity. Therefore, the pure multi-photon picture breaks down. As was mentioned in the introduction, for similar conditions in strong-field single ionization of noble gases, rich momentum space patterns were observed that could not be explained within an MPI picture. Their origin was found in laser-driven scattering of the continuum electron from the Coulomb-field of the ionic core, leading to Ramsauer-Townsend-like interference fringes in the angular distribution [18, 20]. The low-energy distribution around 0.4 eV exhibits a similar behavior since the momentum distribution is smeared out in the radial direction, being close to the fan-like structures characteristic for

the laser-driven electron scattering. Arbo *et al.* [18] give a classical formula for the dominating angular momentum at a given laser field strength F_0, laser angular frequency ω, and momentum p:

$$L(p) = \sqrt{\alpha^2 p^2 + 2\alpha}. \qquad (4)$$

Here L denotes the dominating angular momentum and $\alpha = F_0/\omega^2$. Since no quantities specific to the atomic species enter this equation, it should be universal and indeed proved to be valid for hydrogen and rare gases. Inserting the experimental conditions and the observed momentum in Eq. 4, we obtain a value of $L = 3.96$, in excellent agreement with the observed g-wave character of the low momentum pattern with four minima.

Comparison of the theoretical momentum spectra to the experimental results shows reasonable overall agreement in the cross section pattern, as the underlying methods would imply. Nevertheless, differences persist and neither theory is in really good agreement with the experiment. This concerns both the emission pattern, as shown by the momentum distributions, and the energy spectra, where the relative intensities of the various emission lines and their position can be quantitatively
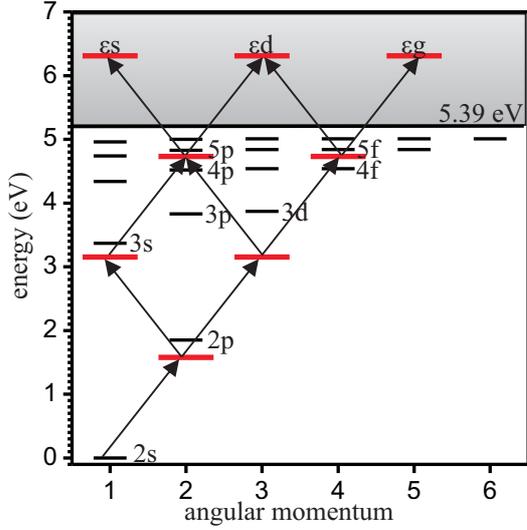
FIG. 6: Energy scheme of lithium including the lowest excited states as well as possible four-photon absorption pathways from the 2s ground state to the continuum.

judged. At the lowest intensity of $I_p = 4 \times 10^{11}$ W/cm^2, both calculations reproduce the main features of the MPI line due to four-photon absorption rather well concerning the radial position and the dominant d-wave angular distribution pattern. Apart from that the strong emission along the laser polarization is better described by the ALM calculation while MIM shows stronger 45° and 90° maxima. This tendency continues for rising laser intensity. In the intermediate intensity regime, the MIM results show slightly weaker maxima along the polarization axis, whereas experimentally up to 3.0×10^{12} W/cm^2 the longitudinal emission is strongest.

The experimentally observed continuous ponderomotive line-shift is not shown by the theories. Instead, they obtain a nearly constant radial position of the MPI line with its intensity being taken over by a newly emerging line at a momentum of about 0.22 a.u. While the ALM results exhibit this effect gradually evolving up to 8×10^{12} W/cm^2, the MIM cross section pattern undergoes this transition abruptly from 8×10^{11} W/cm^2 to 2×10^{12} W/cm^2.

For higher intensities this pattern is rather stable. Interestingly, in the ALM spectra, the NRMPI line which is observed at the lowest intensity at 0.27 a.u. radial momentum, is present up to the highest intensities and does not show the significant variation in position that is clearly seen in the energy spectra (lowest panels in the figures). The corresponding line in the MIM spectra becomes relatively weak and almost disappears above 8×10^{12} W/cm^2. The disagreement with the experimentally observed continuous shift of the MPI line and this behaviour is striking. Experimentally, up to 2×10^{12} W/cm^2 the ion momentum resolution might wash out possible close-lying lines, but starting from 4×10^{12} W/cm^2 the well-resolved electron momentum data clearly do not show the multiple line structure predicted by the ALM calculation. In this respect the MIM predictions are in better agreement with experiment, showing very low intensity
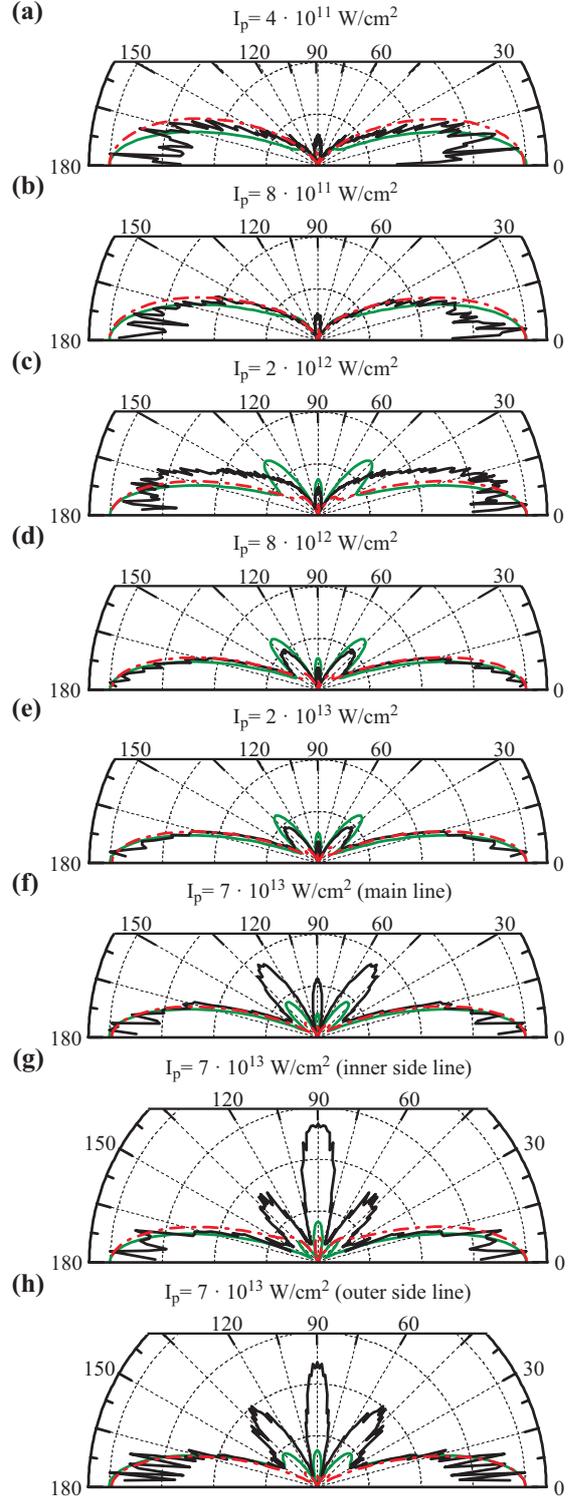
FIG. 7: (a)-(f): Photoelectron angular distributions (PAD) of the main REMPI line for various laser intensities as indicated. The black, green (gray) and dash-dotted red (gray) lines, are the experimental, MIM and ALM results. Panel (g) and (h) show PADs of the side lines in Fig. 5(c) at 0.27 a.u. and 0.18 a.u. momentum, respectively.

at the position of the dashed semicircle.

For the two highest intensities, the high-momentum component of the MPI line, which experimentally is observed at 0.28 a.u., is reproduced quite well by ALM and to a somewhat lesser extent also by MIM. The first-order ATI line for rising intensity also develops a threefold splitting of the forward/backward maxima, which experimentally is best resolved on the left side of Fig. 5(c, top diagram). Here, the differences to the theoretical patterns are subtle. Given the limited experimental resolution and statistical significance, it can be stated that the double splitting of MIM at 8.0×10^{12} W/cm^2 is not observed and that neither theory reproduces the experimental pattern at the highest peak intensity. This is supported by the energy spectra, which show that MIM agrees better in the ATI line positions but their intensity relative to the main line is overestimated. On the other hand, ALM shows better agreement concerning the line strength but disagrees in the line positions, which are higher than observed experimentally.

Finally, a noteworthy feature of the MIM and ALM results is their changing character beyond the over-the-barrier intensity of 3.4×10^{12} W/cm^2. At lower intensities, the semicircular patterns are consistent with the multi-photon absorption mechanism with rather sharp excess energy, whereas at higher intensities, fan-like structures appear. They extend to small radial momentum and are particularly pronounced at $90°$.

In order to quantitatively analyze the results further, the angular distributions PADs for the main MPI line are displayed in Fig. 7 (a) to (f). For the highest intensity, the PADs for both side lines are also shown in panels (g) and (h). The experimental PADs were obtained by summing up the data over particular radial momentum intervals and binning the result over the polar angle. The data were subsequently corrected for the solid angle covered.

As mentioned already in the discussion of the momentum spectra at low intensity the photoelectron angular distribution with maxima along the polarization axis and at $90°$ emission angle is consistent with dominant d-wave emission. The PAD changes with rising intensity, showing increasing strength for the $45°$ lobes characteristic for the g-partial wave. This indicates that ionization through REMPI is governed by the resonance with the $4f$ bound state. In this intensity regime, the MIM model reproduces the $90°$ lobe and also the emerging $45°$ lobes, which are clearly seen at $I_p = 8 \times 10^{12}$ W/cm^2 and $I_p = 2 \times 10^{13}$ W/cm^2. The disagreement at $I_p = 2 \times 10^{12}$ W/cm^2 is most likely due to the reduced experimental angular resolution of the ion momentum spectra smearing out the minima in between the $0°$ lobes and the $45°$ lobes. The ALM results in all these cases show too low magnitudes of these lobes relative to the $0°$ emission. For the highest intensity (f) both calculations underestimate the large-angle lobes not only for the main line but also for the low (g) and high (h) energy side lines. The three lines vary in the relative magnitudes of the angular maxima and, therefore, have a different partial-wave composition.

In light of the differences between experiment and theory, as well as the detailed predictions from the two numerical approaches, we performed a test by modifying the local potential that was used in the MIM approach by a presumably "small"

amount. In that change, the binding energies were modified by about 1% by slightly weakening the local exchange term in the core potential. To our surprise, the results changed significantly and, presumably by accident, sometimes showed strong resemblance to the ALM predictions. While pursuing such tests in more detail goes beyond the scope of the present paper, this check suggests a very high sensitivity of the theoretical predictions on the details of the structure description, resulting in slightly different resonance positions and "stepping stones" provided by the discrete states. The above conclusion regarding the structure dependence is further supported by comparison of our predictions for the atomic hydrogen target. With the known target wave functions and a pure Coulomb potential in this case, the two methods yield excellent agreement in the predicted ejected electron energy spectra, thereby giving us confidence that the time propagation of the initial state in the laser field has been treated with sufficient accuracy in both the MIM and ALM codes.

V. CONCLUSION

In the present study, a new apparatus combining a reaction microscope with a magneto-optically trapped and cooled lithium target was used to explore the dynamics of strong-field ionization of lithium over a wide range of intensities, both experimentally and theoretically. Compared to the frequently studied noble gases, the ionization potential is much lower and thus already four-photon absorption (at 785 nm) is sufficient for ionization. Therefore, ionization is observed for intensities starting from $I_p = 10^{11}$ W/cm^2 and is well understood in terms of multi-photon ionization and above-threshold ionization. Starting at $I_p = 4 \times 10^{12}$ W/cm^2, however, resonance-enhanced multi-photon ionization occurs, which dominates ionization also for higher intensities. While classical over-the-barrier ionization may already occur at $I_p = 3.4 \times 10^{12}$ W/cm^2, no direct manifestation of this effect was found in the ionized electron momentum and energy spectra. Signatures for the breakdown of a perturbative multi-photon absorption description were found in side lines to the main REMPI-lines. They resemble the richly structured momentum spectra observed in the tunneling regime for noble gases.

The experimental data were compared to predictions from numerical solutions of the time-dependent Schrödinger equation within two different approaches set up on a radial grid. Different target potentials and methods for time propagation were employed. To allow for a comparison with the experimental data, the theoretical predictions were averaged over the laser focus volume. While there is overall qualitative agreement between experiment and theory, significant deviations remain in the details, such as the photoelectron angular distribution and the position and intensity evolution of the various MPI and ATI line patterns as a function of the peak intensity. Neither method reproduced the expected ponderomotive shift of the photoelectron lines.

Consequently, despite the ostensible simplicity of multiphoton ionization of lithium, a quasi-one electron atom, accurate theoretical calculations of this reaction are by no means

straightforward. They require a high degree of sophistication, and the results seem to be highly sensitive to small details, particularly in the description of the Li^+ core. We hope that the work presented here will stimulate further studies, both experimentally and theoretically.

If you have acknowledgments, this puts in the proper section head.

[1] M. Protopapas, C. H. Keitel, and P. L. Knight, Reports on Progress in Physics **60**, 389 (1997), URL http://stacks.iop.org/0034-4885/60/i=4/a=001.

[2] P. Lambropoulos, P. Maragakis, and J. Zhang, Physics Reports **305**, 203 (1998), ISSN 0370-1573, URL http://www.sciencedirect.com/science/article/B6TVP-3VN3C7M-2/2/b14544202543d0173ca48cbebcfff9dc.

[3] N. B. Delone and V. P. Krainov, Physics-Uspekhi **41**, 469 (1998), URL http://stacks.iop.org/1063-7869/41/469.

[4] A. Scrinzi, M. Y. Ivanov, R. Kienberger, and D. M. Villeneuve, J. Phys. B **39**, R1 (2006), URL http://stacks.iop.org/0953-4075/39/R1.

[5] L. V. Keldysh, Zh. Eksp. Teor. Fiz. **47**, 1945 (1964).

[6] P. B. Corkum, Phys. Rev. Lett. **71**, 1994 (1993), URL http://link.aps.org/doi/10.1103/PhysRevLett.71.1994.

[7] E. Mevel, P. Breger, R. Trainham, G. Petite, P. Agostini, A. Migus, J.-P. Chambaret, and A. Antonetti, Phys. Rev. Lett. **70**, 406 (1993), URL http://link.aps.org/doi/10.1103/PhysRevLett.70.406.

[8] R. R. Freeman, P. H. Bucksbaum, H. Milchberg, S. Darack, D. Schumacher, and M. E. Geusic, Phys. Rev. Lett. **59**, 1092 (1987), URL http://link.aps.org/doi/10.1103/PhysRevLett.59.1092.

[9] S. Augst, D. Strickland, D. D. Meyerhofer, S. L. Chin, and J. H. Eberly, Phys. Rev. Lett. **63**, 2212 (1989), URL http://link.aps.org/doi/10.1103/PhysRevLett.63.2212.

[10] M. Schuricke, J. Steinmann, G. Zhu, A. Dorn, K. Simeonidis, J. Ullrich, I. Ivanov, and A. S. Kheifets, in *The XI International Conference on Multiphoton Processes* (Heidelberg, Germany, 2008), p. Fr.20, URL https://www.mpi-hd.mpg.de/ICOMP2008/webpdffiles/Fr23.pdf.

[11] G. Petite, F. Fabre, P. Agostini, M. Crance, and M. Aymar, Phys. Rev. A **29**, 2677 (1984), URL http://link.aps.org/doi/10.1103/PhysRevA.29.2677.

[12] B. Yang, K. J. Schafer, B. Walker, K. C. Kulander, P. Agostini, and L. F. DiMauro, Phys. Rev. Lett. **71**, 3770 (1993), URL http://link.aps.org/doi/10.1103/PhysRevLett.71.3770.

[13] M. J. Nandor, M. A. Walker, and L. D. V. Woerkom, J. Phys. B **31**, 4617 (1998), URL http://stacks.iop.org/0953-4075/31/4617.

[14] V. Schyja, T. Lang, and H. Helm, Phys. Rev. A **57**, 3692 (1998), URL http://link.aps.org/doi/10.1103/PhysRevA.57.3692.

[15] A. Rudenko, K. Zrost, C. D. Schröter, V. L. B. de Jesus, B. Feuerstein, R. Moshammer, and J. Ullrich, J. Phys. B **37**, L407 (2004), URL http://stacks.iop.org/0953-4075/37/L407.

[16] C. M. Maharjan, A. S. Alnaser, I. Litvinyuk, P. Ranitovic, and C. L. Cocke, J. Phys. B **39**, 1955 (2006), URL http://stacks.iop.org/0953-4075/39/1955.

[17] Z. Chen, T. Morishita, A.-T. Le, M. Wickenhauser, X. M. Tong, and C. D. Lin, Phys. Rev. A **74**, 053405 (pages 11) (2006), URL http://link.aps.org/abstract/PRA/v74/e053405.

[18] D. G. Arbo, S. Yoshida, E. Persson, K. I. Dimitriou, and J. Burgdorfer, Phys. Rev. Lett. **96**, 143003 (pages 4) (2006), URL http://link.aps.org/abstract/PRL/v96/e143003.

[19] T. Morishita, Z. Chen, S. Watanabe, and C. D. Lin, Phys. Rev. A **75**, 023407 (pages 7) (2007), URL http://link.aps.org/abstract/PRA/v75/e023407.

[20] D. G. Arbó, K. I. Dimitriou, E. Persson, and J. Burgdörfer, Phys. Rev. A **78**, 013406 (pages 6) (2008), URL http://link.aps.org/abstract/PRA/v78/e013406.

[21] M. Nurhuda and F. H. M. Faisal, Phys. Rev. A **60**, 3125 (1999), URL http://link.aps.org/doi/10.1103/PhysRevA.60.3125.

[22] A. N. Grum-Grzhimailo, B. Abeln, K. Bartschat, D. Weflen, and T. Urness, Phys. Rev. A **81**, 043408 (2010), URL http://link.aps.org/doi/10.1103/PhysRevA.81.043408.

[23] T. J. Park and J. C. Light, J. Chem. Phys. **85**, 5870 (1986), URL http://jcp.aip.org/resource/1/jcpsa6/v85/i10/p5870_s1.

[24] G. Zhu, M. Schuricke, J. Steinmann, J. Albrecht, J. Ullrich, I. Ben-Itzhak, T. J. M. Zouros, J. Colgan, M. S. Pindzola, and A. Dorn, Phys. Rev. Lett. **103**, 103008 (2009), URL http://link.aps.org/abstract/PRL/v103/e103008.

[25] J. Ullrich, R. Moshammer, A. Dorn, R. Dorner, L. P. H. Schmidt, and H. Schmidt-Bocking, Reports on Progress in Physics **66**, 1463 (2003), ISSN 0034-4885, URL http://www.iop.org/EJ/abstract/0034-4885/66/9/203/.

[26] H. J. Metcalf and P. van der Straten, *Laser Cooling and Trapping (Graduate Texts in Contemporary Physics)*

(Springer, 2001), ISBN 0387987282, URL http://www.amazon.com/exec/obidos/redirect?tag=citeulike07-20\&path=ASIN/0387987282.

[27] A. S. Alnaser, X. M. Tong, T. Osipov, S. Voss, C. M. Maharjan, B. Shan, Z. Chang, and C. L. Cocke, Physical Review A **70**, 023413 (2004), URL http://link.aps.org/abstract/PRA/v70/e023413.

[28] A. Goldberg, H. M. Schey, and J. L. Schwartz, American Journal of Physics **35**, 177 (1967), URL http://link.aip.org/link/?AJP/35/177/1.

[29] A. N. Grum-Grzhimailo, A. D. Kondorskiy, and K. Bartschat, J. Phys. B **39**, 4659 (2006), URL http://stacks.iop.org/0953-4075/39/i=22/a=010.

[30] K. Bartschat, *Computational Atomic Physics* (Springer-Verlag (Heidelberg, New York), 1996).

[31] A. K. Kazansky and N. M. Kabachnik, Journal of Physics B: Atomic, Molecular and Optical Physics **41**, 135601 (2008), URL http://stacks.iop.org/0953-4075/41/i=13/a=135601.

[32] A. Sarsa, F. J. Galvez, and E. Buendia, At. Data Nucl. Data Tables **88**, 163 (2004), URL http://www.sciencedirect.com/science/article/B6WBB-4D7CCCM-1/2/4aac5695d2170326a9834bb19540d0b1.

[33] A. Sarsa, F. J. Galvez, and E. Buendia, Journal of Physics B: Atomic, Molecular and Optical Physics **36**, 4393 (2003), URL http://stacks.iop.org/0953-4075/36/i=22/a=002.

[34] X. Antoine, A. Arnold, C. Besse, M. Ehrhardt, and A. Schädle, Commun. Comput. Phys. **4**, 729 (2008).

[35] S. Augst, D. D. Meyerhofer, D. Strickland, and S. L. Chint, Journal of the Optical Society of America B **8**, 858 (1991), URL http://josab.osa.org/abstract.cfm?URI=josab-8-4-858.

[36] T. Nubbemeyer, K. Gorling, A. Saenz, U. Eichmann, and W. Sandner, Phys. Rev. Lett. **101**, 233001 (2008), URL http://link.aps.org/doi/10.1103/PhysRevLett.101.233001.

[37] In literature the name COLTRMS (COLd Target Recoil Ion Momentum Spectroscopy) is equivalently used for REMI